nature communications



Article

https://doi.org/10.1038/s41467-022-32836-6

Step-by-step state-selective tracking of fragmentation dynamics of water dications by momentum imaging

Received: 27 January 2022

Accepted: 17 August 2022

Published online: 01 September 2022

Check for updates

Travis Severt^{1,8}, Zachary L. Streeter^{2,3,8}, Wael Iskandar^{2,8}, Kirk A. Larsen^{2,4}, Averell Gatton^{2,5}, Daniel Trabert 6, Bethany Jochim, Brandon Griffin 6, Bethany Brandon 6, Bethany Brandon 6, Bethany Brandon 6, Bethany Brandon 6, Bethan Elio G. Champenois^{2,4}, Matthew M. Brister², Dylan Reedy⁷, Demitri Call⁷, Richard Strom^{2,5}, Allen L. Landers⁵, Reinhard Dörner 6, Joshua B. Williams⁷, Daniel S. Slaughter ^{® 2}, Robert R. Lucchese ^{® 2}, Thorsten Weber ^{® 2} ⊠, C. William McCurdy^{2,3} A Itzik Ben-Itzhak ¹

The double photoionization of a molecule by one photon ejects two electrons and typically creates an unstable dication. Observing the subsequent fragmentation products in coincidence can reveal a surprisingly detailed picture of the dynamics. Determining the time evolution and quantum mechanical states involved leads to deeper understanding of molecular dynamics. Here in a combined experimental and theoretical study, we unambiguously separate the sequential breakup via D⁺ + OD⁺ intermediates, from other processes leading to the same $D^+ + D^+ + O$ final products of double ionization of water by a single photon. Moreover, we experimentally identify, separate, and follow step by step, two pathways involving the $b^{1}\Sigma^{+}$ and a $^{1}\Delta$ electronic states of the intermediate OD⁺ ion. Our classical trajectory calculations on the relevant potential energy surfaces reproduce well the measured data and, combined with the experiment, enable the determination of the internal energy and angular momentum distribution of the OD⁺ intermediate.

The measurement of reaction dynamics occurring on the femtosecond time scale has long been the target of various kinds of time-resolved spectroscopies and, more recently, has been accomplished with ultrafast X-ray measurements. Those measurements have exploited pump-probe strategies¹, transient absorption², and time-resolved X-ray scattering^{3,4}, among other methods. Combining time-resolved X-ray measurements with momentum imaging coincidence detection⁵⁻⁷ that gives direct access to state-selective ionization and detailed insight into dissociation dynamics in the molecular frame remains a challenge. Recent interest in such time-resolved spectroscopies extends to the IR, UV and VUV regimes⁸⁻¹².

Although it would seem intuitive that time resolution is necessary to see the steps in the unimolecular reactions that have frequently been the subjects of momentum imaging coincidence experiments, it was demonstrated that such experiments, without time-resolved X-ray or laser pulses, can in fact be used to distinguish the steps in a sequential reaction¹³⁻²¹. Recently, the nativeframes analysis method was introduced21,22, and the authors

¹J. R. Macdonald Laboratory, Physics Department, Kansas State University, Manhattan, KS 66506, USA. ²Chemical Sciences Division, Lawrence Berkeley National Laboratory, Berkeley, CA 94720, USA. 3Department of Chemistry, University of California, Davis, CA 95616, USA. 4Graduate Group in Applied Science and Technology, University of California, Berkeley, CA 94720, USA. 5Department of Physics, Auburn University, Auburn, AL 36849, USA. 6Institut für Kernphysik, Goethe-Universität, Max-von-Laue-Straße 1, 60438 Frankfurt am Main, Germany. Department of Physics, University of Nevada Reno, Reno, NV 89557, USA. ⁸These authors contributed equally: Travis Severt, Zachary L. Streeter, and Wael Iskandar contributed equally by leading the data analysis, theoretical, and experimental aspects of the ALS campaign, respectively. Me-mail: TWeber@lbl.gov; cwmccurdy@lbl.gov; ibi@phys.ksu.edu

showed that photo-induced momentum imaging observations can resolve the sequence of events in the dissociation of a molecule involving vibrational and rotational dynamics following multiple ionization.

Here, the goal is to take a step further by combining such measurements with detailed ab initio theoretical calculations of the multiple Born–Oppenheimer potential surfaces governing such a reaction and the nuclear dynamics on those surfaces. With this methodology, the spectral signatures of the steps of a reaction, including non-adiabatic transitions that occur in those steps, can be identified experimentally. The expected result is a clear picture, not only of the steps, but of the electronic states of the transients involved in them.

In the present work, we accomplish the goal stated above. Specifically, we track sequential fragmentation step-by-step, by combining a kinematically complete measurement of all reaction products following single-photon absorption, computing the classical trajectories on the relevant potential-energy surfaces, and employing the native-frames analysis to separate the measured data into the steps of the process. Moreover, we are able to observe the internal-energy distribution of the intermediate molecule, which has sufficient energy to predissociate—demonstrating the power of the presented methodology.

Results

Sequential fragmentation of water

To explore the molecular dynamics causing sequential fragmentation we study, as a test case, the heavy water molecule that fragments into $D^+ + D^+ + O(^3P) + 2e^-$ following the absorption of a single photon. We focus on sequential fragmentation via an OD^+ intermediate, which follows the steps listed below

$$D_2O^{2+} \rightarrow D_I^+ + OD_{II}^+ \quad (Step \, 1) \eqno(1)$$

$$OD_{II}^{+} \rightarrow D_{II}^{+} + O(^{3}P)$$
 (Step 2). (2)

Note that the D^+ fragments are labeled I and II according to their ejection order in the sequential process, i.e., labeled by their fragmentation step according to Eq. (1) and Eq. (2), respectively (a notation used throughout). Despite the fact that these D atoms are indistinguishable, we show below that the sequential breakup step, i.e., the ejection order, can be associated with each detected D^+ fragment.

It was suggested by Streeter et al.²³, who identified many measured concerted fragmentation paths in H_2O^{24} , that one of the reaction pathways leading to the $H^+ + H^+ + O(^3P)$ final state involves sequential breakup via an OH^+ intermediate. Specifically, they speculated that a feature in the data, having broad angular spread between the protons' ejection directions, may be due to transitions involving the $2\,^{1}A_1$ state of the water dication, which undergoes two-body breakup to $H^+ + OH^+(b\,^{1}\Sigma^+)$. This $b\,^{1}\Sigma^+$ state of OH^+ is known to predissociate into $OH^+ + O(^3P)$ via a crossing with the OH^+ is known to predissociate into $OH^+ + O(^3P)$ via a crossing with the OH^+ is known to predissociate into $OH^+ + O(^3P)$ via a crossing with the OH^+ is known to predissociate into $OH^+ + O(^3P)$ via a crossing with the OH^+ is known to predissociate into $OH^+ + O(^3P)$ via a crossing with the OH^+ is known to predissociate into $OH^+ + O(^3P)$ via a crossing with the OH^+ is known to predissociate into $OH^+ + O(^3P)$ via a crossing with the OH^+ is known to predissociate into $OH^+ + O(^3P)$ via a crossing with the OH^+ is known to predissociate into $OH^+ + O(^3P)$ via a crossing with the $OH^+ + O(^3P)$ via a crossing wi

First fragmentation step

The first step in sequential breakup requires one O–D_I bond to break, while the OD_{II}⁺ fragment remains bound. In Fig. 1a, we show a cut of the relevant potential energy surfaces (PES) of D₂O²⁺ leading to D_I⁺ + OD_{II}⁺ breakup along the dissociation of one D⁺ at the equilibrium bond angle of neutral water, which is the relevant angle in the Franck-Condon approximation. These states of D₂O²⁺ correlate with the b $^1\Sigma^+$ and a $^1\Delta$

states of OD^+ , which are predissociative via a crossing with the $A^3\Pi$ state of OD^+ .

Figure 1b displays cuts in a few PES of $D_2O^{2^+}$ for the same bond angle, but when one D_I^+ is at 1000 a.u. and therefore its interaction with the remaining OD_{II}^+ is negligible. These cuts are effective radial potentials for fixed J of the OD_{II}^+ states correlating with the $D_{II}^+ + O(^3P)$ and $D_{II}^+ + O(^1D)$ dissociation limits, which are involved in the predissociation of the intermediate OD_{II}^+ molecule.

Second fragmentation step

The essence of the second step of the sequential fragmentation revealed in our experiment is the dissociation of the OD_{II}^+ ion produced in the first step in its $b^1\Sigma^+$ and $a^1\Delta$ states by a spin-orbit induced transition to the $A^3\Pi$ state. Only if the OD_{II}^+ ion is produced in rovibrationally excited states above the effective radial barrier to the dissociation limit of the $A^3\Pi$ state, shown in Fig. 1b, can it be predissociated by this transition, and these dynamics leave clear signatures in the momenta of the final products.

Using the PES information detailed above, we model the reaction dynamics by the propagation of ensembles of classical trajectories on the relevant potential surface for a few picoseconds, at which time the $\mathrm{OD}_{\mathrm{II}}^+$ population is evaluated. We assume that all $\mathrm{OD}_{\mathrm{II}}^+$ ions with internal energy above the $\mathrm{D}_{\mathrm{II}}^+ + \mathrm{O}(^3P)$

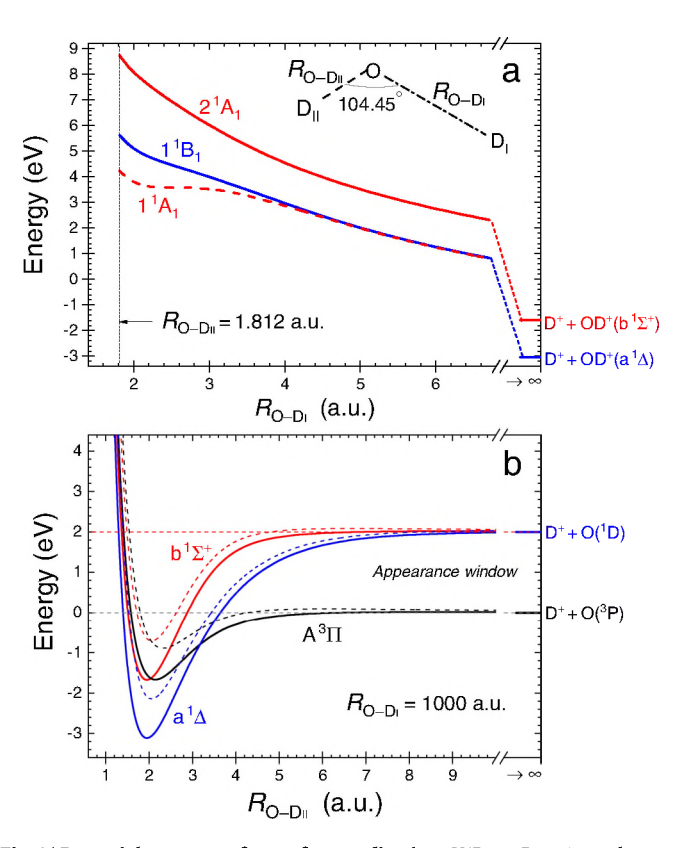


Fig. 1 | **Potential energy surfaces of water dication,** $V(R_{O-D_1}R_{O-D_n})$, **at the equilibrium angle.** Cuts through the potential energy surfaces, relevant for sequential fragmentation of $D_2O^{2^+}$ via OD_{11}^+ intermediate, showing **a** the asymmetric stretch of $D_2O^{2^+}$ for a fixed bond angle (104.45') and internuclear distance $(R_{O-D_n}=1.812 \text{ a.u.})$ of the other O–D bond for the three states of $D_2O^{2^+}$ that produce the diatomic intermediate which further dissociates (see text), and **b** the OD_{11}^+ potentials when the interaction with the other D_1^+ is negligible $(R_{O-D_1}=1000 \text{ a.u.})$, where solid lines are for J=0, while the effective radial potentials for J=30 are shown as dashed lines. The states in (a) plotted as solid blue and solid red curves produce the diatomic ion with enough internal energy to predissociate via the A $^3\Pi$ state. The energy scale is relative to the $D^++D^++O(^3P)$ dissociation limit. Note that on this energy scale the asymmetric stretch limits for the $1^{11}B_1$ and $2^{11}A_1$ states are -3.021 and -1.619 eV, respectively. Source data are provided as a Source Data file.

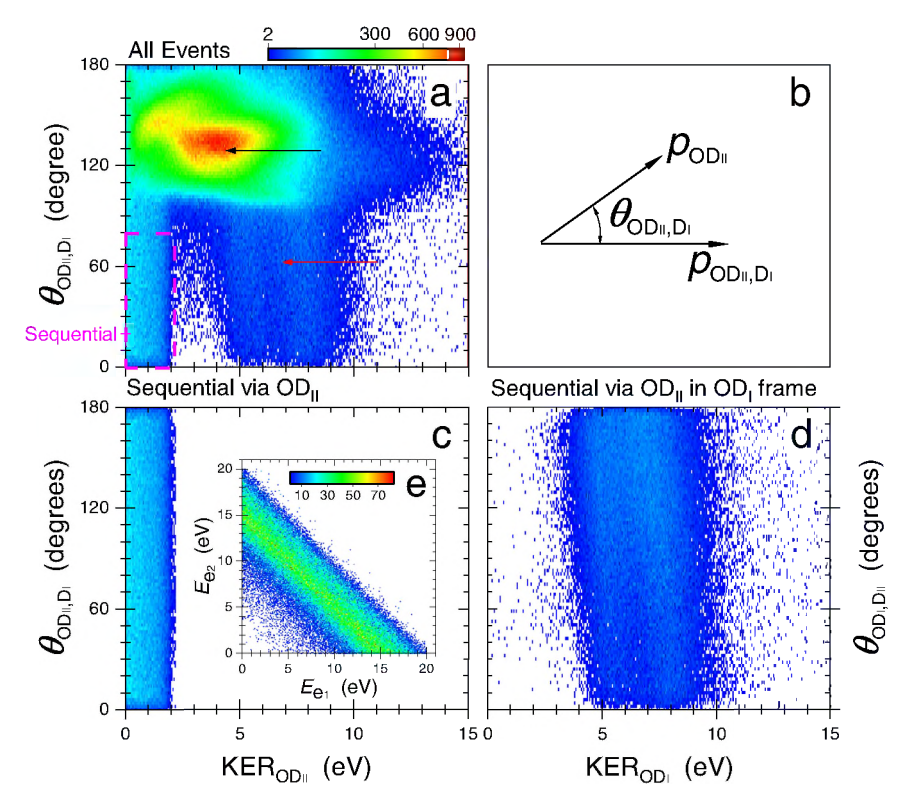


Fig. 2 | **Native frames analysis of D**⁺ + **D**⁺ + **O breakup. a** All the measured D⁺ + D⁺ + O events (shown using a $\sqrt{\text{counts}}$ scale) as a function of the kinetic energy released upon OD_{11}^+ dissociation, $KER_{OD_{11}^+}$, and the angle between the conjugate momenta, θ_{OD_{11},D_1} . Sequential fragmentation events via D_1^+ + OD_{11}^+ are identified (see text) by the uniform angular distribution within the magenta-dashed rectangle (i.e., $KER_{OD_{11}} < 2.3$ eV and $O^\circ < \theta_{OD_{11},D_1} < 80^\circ$). **b** Schematic diagram of the conjugate momenta and the angle between them (see Eqs. (5) and (6) in the "Methods" section). Sequential breakup via OD_{11}^+ analyzed in the **c** OD_{11}^+ and **d** OD_1^+ frames, i.e., the correct and wrong fragmentation-step order of the D⁺ fragments, respectively (see text). As detailed in the "Methods" section, analysis of the events in the wrong

reference frame, as is the case shown in panel (**d**) and indicated by the different axis labels (KER_{OD1} and θ_{OD_1,D_1}), yields a distribution significantly different than the one expected for sequential fragmentation^{21,22}, specifically, a non-uniform angular distribution, a KER_{OD1} that depends on the angle θ_{OD_{11},D_1} , and a much higher than expected KER_{OD1}. This sequential fragmentation distribution, analyzed in the wrong D* ejection order, is marked by a red arrow in panel (**a**), while concerted breakup is indicated by a black arrow. **e** Energy-correlation map of the ionized electrons associated with sequential fragmentation via D₁+ + OD₁+ (shown as counts). Source data are provided as a Source Data file.

dissociation limit and zero rotational energy, i.e., between the two horizontal dashed lines in Fig. 1b labeled appearance window, predissociate to D_{ll}^+ + O fragments within a few picoseconds due to spin-orbit coupling with the A $^3\Pi$ state 25,26 . Nonzero rotational angular momentum adds a centrifugal barrier to this picture for all three states of OD_{ll}^+ in Fig. 1b, modifying the appearance window, and leaving a clear signature of rotational excitation in the kinetic energy of the atomic fragments produced by this mechanism, as we discuss below.

Fragmentation experiment and analysis

To explore the sequential-breakup mechanism experimentally, we initiate fragmentation by the absorption of a 61 eV photon, thereby producing a doubly-ionized water molecule at a well-defined energy (24.1 eV) above the lowest dissociation limit, D⁺ + D⁺ + O(³P). We measure all four charged fragments in coincidence and determine their final momenta using a cold target recoil ion momentum spectroscopy (COLTRIMS) technique⁵⁻⁷. Specifically, we focus on events producing two electrons, two deuterons, and a neutral oxygen whose final momentum is evaluated using momentum conservation.

We analyze the three-body fragmentation assuming an OD_{ll}^{11} intermediate using the native frames method^{21,22}. In our present case, shown schematically in Fig. 2b, the conjugate momenta (of the Jacobi coordinates) associated with the first and second breakup steps are $p_{OD_{ll},D_{ll}}$ and $p_{OD_{ll}}$, respectively, while $\theta_{OD_{ll},D_{ll}}$ is the angle between them—all defined in the "Methods" section.

Identifying sequential fragmentation of water

Rotation of the intermediate diatomic ion in the fragmentation plane provides a clear signature of sequential fragmentation^{15-18,21,22,27}. In the native frames analysis this rotation manifests itself as a nearly uniform $N(\theta_{\mathrm{OD}_{11},\mathrm{D}_1})$ angular distribution if the predissociation lifetime is long enough so the rotation of OD_{11}^+ wipes out any initial angular preference. As detailed in the "Methods" section, in Fig. 2a we show the distinct uniform angular distribution of sequential fragmentation via $\mathrm{D}_1^+ + \mathrm{OD}_{11}^+$ (marked by the dashed-magenta rectangular boundary), which occurs at the expected kinetic energy release (KER) of OD_{11}^+ dissociation²⁵, indicated by the appearance window in Fig. 1b.

Three observations are appropriate at this point: First, in Fig. 2c we show the complete angular distribution of this sequential-fragmentation channel of D_2O^{2+} , which was reconstructed taking advantage of the fact that $N(\theta_{OD_n,D_1})$ is nearly uniform^{21,22}.

Second, one can associate each detected D^+ with the relevant fragmentation step using the native frames analysis, as described in the "Methods" section. After correctly assigning which D^+ comes from the OD^+ intermediate, we combine the data for all plots presented below, i.e., we use all sequential events via OD_{II}^+ .

Finally, we note that the high degree of rotational excitation in the intermediate OD_{ll}^+ b $^l\Sigma^+$ and $a^l\Delta$ states found in the classical trajectory simulation, which leads to the signature of sequential breakup, has its origin in the strong force towards bond opening on the corresponding 2^lA_l and lB_l potential surfaces of D_2O^{2+} upon the loss of two electrons. In the simplest picture of the electronic structure of water, these states

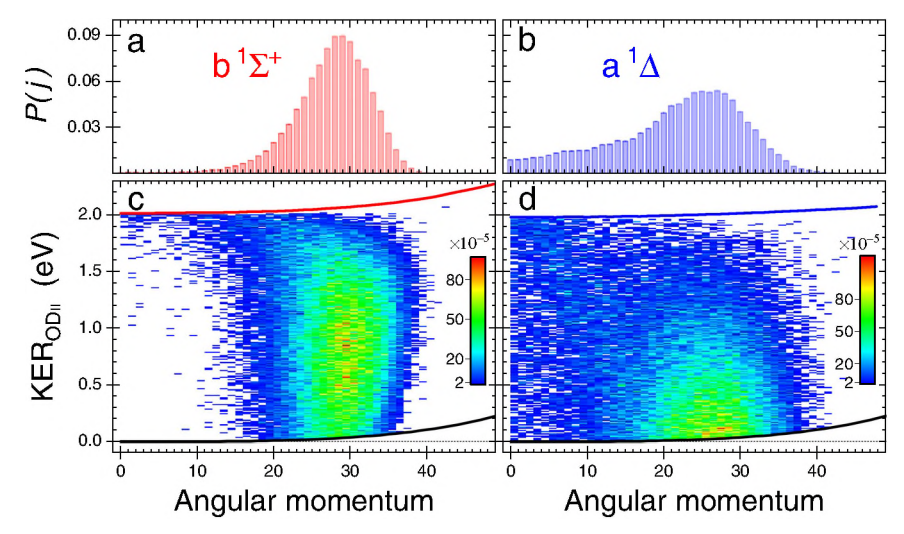


Fig. 3 | **Normalized angular momentum distributions.** These P(J) distributions $(\Sigma_J P(J) = 1)$ are computed for the **a** b $^1\Sigma^*$ and **b** a $^1\Delta$ states of OD* populated during $D_2O^{2^*}$ fragmentation (see text). Calculated angular momentum—KER_{OD_{II}} correlation maps for the **c** b $^1\Sigma^*$ and **d** a $^1\Delta$ states. The lines in panels **c** and **d** represent the modification of the appearance window in Fig. 1b for nonzero rotational angular

momentum by the addition of a centrifugal potential to both the singlet and triplet potential curves (specifically, A ${}^3\Pi$ · black, b ${}^1\Sigma^*$ · red, and a ${}^1\Delta$ · blue). In the absence of tunneling no dissociating trajectories can appear outside these lines. Source data are provided as a Source Data file.

are created by the loss of two lone-pair electrons. From simple molecular orbital considerations, losing one or two electrons out of the inplane $3a_1$ lone-pair orbital should lead to an opening of the bond. Streeter et al.²³ found that this torque is strong enough to cause the two D⁺ fragments, ejected initially near the 104° equilibrium bond angle in a concerted three-body fragmentation on these surfaces, to invert this angle to greater than 180° while they are still close to the oxygen atom. Similarly, trajectories leading to the two-body breakup into $D_{I}^{+} + OD_{II}^{+}$ impart a strong torque on the OD_{II}^{+} fragment, resulting in high rotational excitation. Gervais et al.26 also found high rotational excitation in diatomic ion fragments from HOD having insufficient internal energy to predissociate, with the highest being from these two dication states. For the trajectories that produce the OD_{II} fragment with enough internal energy to predissociate via the A ³Π state, in our classical trajectory calculations these dynamics lead to angular momentum distributions peaking near J = 30 as shown in Fig. 3, i.e., even higher levels of rotational excitation than in ref. 26. We note that the angular distribution of the $a^{1}\Delta$ state extends down to J = 0, while the $b^{1}\Sigma^{+}$ state of OD_{II}^{+} cannot be produced rotationally cold. Moreover, this rotational distribution leaves its signature in the kinetic energies of the atomic fragments after dissociation as we discuss further below.

Dissociation limit of sequential fragmentation of water

First, we confirm that the selected sequential fragmentation events lead to the expected $D^+ + D^+ + O(^3P)$ dissociation limit. To that end, in Fig. 4 we present all the measured $D^+ + D^+ + O + 2e^-$ events (red-solid line), resulting from the absorption of a single 61 eV photon, as a function of the total energy release, i.e., $E_{\text{release}} = \text{KER} + E_{e_1} + E_{e_2}$, where E_{e_1} or E_{e_2} is the kinetic energy of an electron in the continuum. Essentially, the measured E_{release} provides information about the dissociation limit, thus allowing one to determine the internal energy of the oxygen fragment. We evaluated the expected value of $E_{release}$ for each dissociation limit from the known photon energy, the complete dissociation energy of water, and the initial state (i.e., ground state) of the heavy water molecule—those locations are marked by vertical lines and labeled by the oxygen final state in Fig. 4—though with a small shift down, ~0.4 eV, due to experimental uncertainties (see 'Experimental method' in the "Methods" section for details). It is evident from the figure that the likelihood of fragmentation to the lowest two dissociation limits, i.e., O(3P) and O(1D), is approximately equal, and each

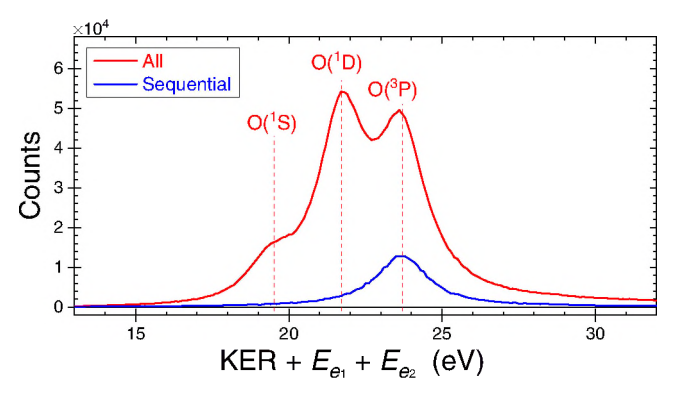


Fig. 4 | **Total energy release in double photoionization of water.** The measured distribution, $N(\text{KER} + E_{e_1} + E_{e_2})$. The vertical lines indicate the expected energy of each $D^+ + D^+ + O$ dissociation limit, which are labeled by the final state of the oxygen atom and shifted down by 0.4 eV (see text). Note that sequential fragmentation via OD_{11}^+ correlates only with the $D^+ + D^+ + O(^3P)$ dissociation limit. The broad energy distribution, clearly visible in the sequential breakup, is mainly due to the extended target along the light-propagation direction, energy resolution, and the spread in center-of-mass momentum that cannot be corrected for because the neutral oxygen fragment is not detected but rather evaluated from momentum conservation. Source data are provided as a Source Data file.

of them is more likely than a breakup to the $O(^1S)$ limit²⁴. In the same figure we also plot (blue line) the sequential events via OD^+ , selected by $KER_{OD_{II}} < 2.3$ eV (see 'Native frames analysis' in the "Methods" section). Figure 4 clearly shows that the sequential fragmentation via OD_{II}^+ leads solely to the $D^+ + D^+ + O(^3P)$ dissociation limit. We also note that the electrons associated with this sequential breakup exhibit an energy sharing that is typical for direct double ionization involving no autoionization, as shown in Fig. 2e.

Sequential fragmentation pathways

As mentioned briefly in the introduction, Streeter et al.²³ suggested that the $OD_{II}^+(b^1\Sigma^+)$ is the intermediate state that predissociates, due to spin-orbit coupling with the $A^3\Pi$ state (shown in Fig. 1b)^{25,26}, into $D_{II}^+ + O(^3P)$ a few picoseconds after the $D_2O^{2^+}$ breaks into $D_{II}^+ + OD_{II}^+(b^1\Sigma^+)$. Inspection of Fig. 1a indicates that the $b^1\Sigma^+$ state

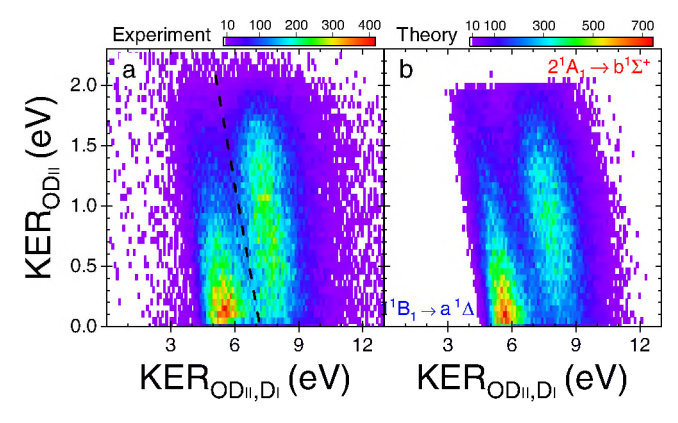


Fig. 5 | **The KER correlation maps of sequential fragmentation of water dications.** The measured yield of D_2O^{2+} breakup into $D^+ + D^+ + O(^3P)$ as a function of KER_{OD₁₁,D₁₁} and KER_{OD₁₁}: **a** Experiment and **b** Theory. The two panels nicely match each other, aided by the choice of similar statistics in the theory to match the experimental data quality. The black-dashed line in panel (**a**) is used to separate the two sequential fragmentation paths (see text), specifically $2^{-1}A_1 \rightarrow b^{-1}\Sigma^+$ (right) from $1^{-1}B_1 \rightarrow a^{-1}\Delta$ (left). This visualization of our pathway separation method, though correct, is simplified in practice by plotting the same data as a function of KER_{OD₁₁,D₁} + KER_{OD₁₁} and KER_{OD₁₁,D₁} - KER_{OD₁₁}, i.e., a 45° rotation of the spectrum in panel (**a**). Then, we project it onto the KER = KER_{OD₁₁,D₁} + KER_{OD₁₁} axis and associate events larger (smaller) than KER = 7.18 eV with the $b^{-1}\Sigma^+$ (or $a^{-1}\Delta$) channel (further details and the KER distributions are provided in Supplementary Note 1). Source data are provided as a Source Data file.

of OD_{II}^+ correlates with the 2 1A_1 state of $D_2O^{2^+}$. If the latter state is populated by a vertical transition from the D_2O ground state (i.e., removing two electrons without changing the internuclear distances or bond angle, which is a reasonable approximation for ionization by a single photon), then a KER of about 7 eV is expected in the first fragmentation step, $D_1^+ + OD_{II}^+$ (b $^1\Sigma^+$), en route to $D^+ + D^+ + O(^3P)$.

To verify this suggested pathway we plot in Fig. 5a the measured sequential fragmentation events selected by $\mathsf{KER}_{\mathsf{OD}_1} < 2.3 \, \mathsf{eV}$, (see 'Native frames analysis' in the "Methods" section for details) leading to $\mathsf{D}^+ + \mathsf{D}^+ + \mathsf{O}(^3\mathsf{P})$ as a function of $\mathsf{KER}_{\mathsf{OD}_1,\mathsf{D}_1}$ and $\mathsf{KER}_{\mathsf{OD}_1}$, i.e., the KER in the first and second fragmentation steps, respectively. One can clearly see the feature centered about the expected $\mathsf{KER}_{\mathsf{OD}_1,\mathsf{D}_1}$ with a broad, relatively flat, $\mathsf{KER}_{\mathsf{OD}_1}$ distribution extending to about 2.1 eV. This clearly affirms the predicted sequential fragmentation path $\mathsf{D}_2\mathsf{O}^{2^+}(2^{-1}\mathsf{A}_1) \to \mathsf{D}_1^+ + \mathsf{OD}_1^+$ (b $^1\Sigma^+$) followed by OD_1^+ (b $^1\Sigma^+$) $\to \mathsf{D}_1^+ + \mathsf{O}(^3\mathsf{P})$.

Note that there is a prominent second feature in Fig. 5a centered on a lower $\mathsf{KER}_{\mathsf{OD}_1,\mathsf{D}_1}$ of about 5.5 eV. This is unexpected, considering the suggestion of Streeter et al.²³ that a single electronic state is involved in sequential fragmentation. Moreover, the $\mathsf{KER}_{\mathsf{OD}_1}$ distribution of this feature peaks near zero and tails off rapidly. These distinct features suggest different fragmentation pathways.

Examination of the potential energy along the asymmetric stretch coordinate, shown in Fig. 1a, indicates that the 1 $^{1}B_{1}$ state of the dication, at the equilibrium $R_{\mathrm{OD}_{1}}$ of water (1.812 a.u.), is about 5.5 eV above the D $^{+}$ + D $^{+}$ + O(^{3}P) dissociation limit associated with the first fragmentation step, D_{1}^{+} + OD $_{11}^{+}$ (a $^{1}\Delta$). Therefore, we attribute this lower KER $_{\mathrm{OD}_{11},D_{1}}$ feature to sequential fragmentation initiated by double ionization to the 1 $^{1}B_{1}$ state, which is consistent with the results of our classical trajectories on the 1 $^{1}B_{1}$ potential surface. This state, then, dissociates into D_{1}^{+} + OD $_{11}^{+}$ (a $^{1}\Delta$). Later, the a $^{1}\Delta$ state predissociates into D_{11}^{+} + O(^{3}P) due to its spin-orbit coupling with the A $^{3}\Pi$ state of OD $_{11}^{+}$. We are not aware of a reported lifetime for the a $^{1}\Delta$ state, however we expect it to be similar to that of the b $^{1}\Sigma^{+}$ state given that both are coupled to the A $^{3}\Pi$ state, and their spin-orbit matrix elements have similar magnitudes according to calculations by de Vivie et al. 25 . In summary, we have discovered another sequential

fragmentation path, namely $D_2O^{2+}(I^1B_1) \rightarrow D_I^+ + OD_{II}^+(a^1\Delta)$ followed by $OD_{II}^+(a^1\Delta) \rightarrow D_{II}^+ + O(^3P)$.

State-selective separation of fragmentation pathways

In Fig. 5 we also compare the measured and simulated KER-correlation maps to each other. In this simulation, we assumed that the cross sections for double ionization are the same for the $2\,^{1}A_{1}$ and $1\,^{1}B_{1}$ states. Both features in the figure match very well, suggesting that our classical trajectory approach, though it approximates the nonadiabatic dynamics, captures the essence of the physical process. Moreover, the measured KER-correlation map enables separation between the two sequential-fragmentation pathways, thus allowing their direct comparison without recourse to theory. This separation is accomplished by selecting events to the right ($2\,^{1}A_{1} \rightarrow b\,^{1}\Sigma^{+}$) or left ($1\,^{1}B_{1} \rightarrow a\,^{1}\Delta$) of the black-dashed line shown in Fig. 5a. Note that this line is tilted reflecting a constant KER (specifically, we used 7.18 eV in the analysis).

Our classical trajectory calculations propagate the same number of trajectories on each dication surface, with no regard to the cross section for producing that dication state in double photoionization. As a result, those calculations can accurately reflect the branching ratios between two- and three-body breakup channels on each electronic state, but provide no information about the photoionization cross sections. In contrast, the experiment does determine the ratio between the two, thus providing a test of the relative magnitudes of the cross sections to be determined by future double photoionization calculations.

Step-by-step comparison of measured and simulated KER

In Fig. 6 we compare the measured and calculated KER distributions for both steps of each sequential fragmentation path. Because the experiment measures the relative cross sections, we scale the theory with an overall factor determined by a least squares fit to preserve the measured information on the relative likelihood of the two sequential fragmentation paths. Note that the calculated KER distribution associated with the $2\,^1\!A_1 \rightarrow b\,^1\!\Sigma^+$ path is scaled by a factor that is 1.17 times larger than the scaling factor used to normalize the $1\,^1\!B_1 \rightarrow a\,^1\!\Delta$ path, as indicated in Fig. 6. This difference is mainly due to the relative magnitudes of the cross sections for double photoionization by a single 61 eV photon landing on the $2\,^1\!A_1$ and $1\,^1\!B_1$ states of $D_2O^{2^+}$.

At a glance, the calculated and measured KER distributions associated with the $D_2O^{2+} \ni D_l^+ + OD_{ll}^+$ breakup, shown in Fig. 6a, match each other nicely. However, a careful inspection shows that the calculated distributions are shifted up by about 0.15 eV. We suspect that this difference stems from approximating the initial wave function of D_2O , which is projected to the D_2O^{2+} states, by a product of normal mode harmonic oscillators instead of a more accurate representation including the effects of the anharmonicity in the ground state PES. Similar discrepancies have been observed in H_2 and were corrected by using a Morse potential to represent the initial state 28 .

The calculated and measured KER distribution associated with the second fragmentation step, namely $OD_{ll}^{+} \rightarrow D_{ll}^{+} + O$ shown in Fig. 6b, match very well for both sequential fragmentation paths. The differences between the KER distributions associated with these two fragmentation paths, noticeable in Fig. 5, become more apparent. The sequential fragmentation via the $b^{\,1}\Sigma^{+}$ state yields a broad, relatively flat, KER distribution peaked around 0.9 eV, while the fragmentation via the a $^{\,1}\Delta$ state peaks at much lower KER, $\sim\!0.15\,\text{eV}$, and falls off rapidly with increasing KER. The fact that the classical trajectory analysis faithfully reproduces the details of these distributions is a strong verification of its validity and the accuracy of the potential surfaces on which it is based.

Internal energy of the intermediate OD₁₁ fragment

It is important to note that the KER in the predissociation of the OD_{\parallel}^{1} images the internal energy of this diatomic ion above the $O(^{3}P)$

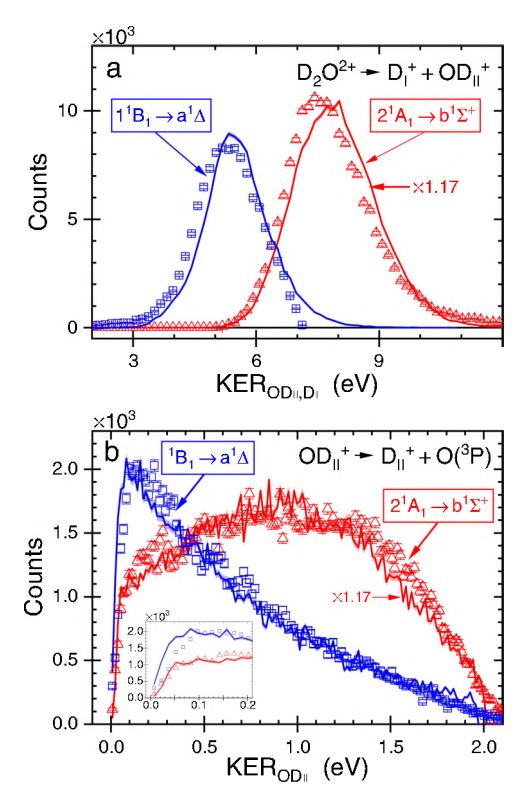


Fig. 6 | **The KER distribution in each breakup step of water dications.** The yield of sequential fragmentation of $D_2O^{2^+}$ into $D^+ + D^+ + O(^3P)$ as a function of **a** KER_{ODu}, D_u and **b** KER_{ODu} (Inset: Zoom-in of low energy range). Comparison of experiment (symbols and statistical error bars) and normalized theory (solid lines, with shaded range marking the simulation's statistical errors) for the two fragmentation pathways (and associated states) identified and separated using Fig. 5a (see text and Supplementary Note 1). As indicated on the figure, the theory scaling of one path is a factor of 1.17 larger than the other one (see text). The high energy cutoff in the measured D_0 to D_0 data in the upper panel is likely due to the imperfect separation of the two channels by the black-dashed line in Fig. 5. Source data are provided as a Source Data file.

dissociation limit, i.e., the internal energy stored in highly excited rovibrational states. This assertion is correct if the assumption, used in our modeling, that all rovibrational states dissociate when their energy exeeds the effective potential barrier leading to the $D_{II}^+ + O(^3P)$ dissociation limit, is valid. The comparison of experiment and theory in Fig. 6b validates that assumption. The remaining population, in the lower rovibrational states of the a $^1\Delta$ and b $^1\Sigma^+$ states of OD_{II}^+ , is measured as the dominant two-body breakup, $D_I^+ + OD_{II}^+$ (see previous reports on $H_2O)^{23,24}$.

Angular momentum of the intermediate OD_{ll}^+ molecule

In addition to the internal energy of the $\mathrm{OD}_{\mathrm{II}}^+$ ion, our classical trajectory simulations provide the angular momentum distribution, P(J), of each state of $\mathrm{OD}_{\mathrm{II}}^+$ shown in Fig. 3. Similar to the KER distributions, here too the P(J) distributions of the a ${}^{\mathrm{I}}\Delta$ and b ${}^{\mathrm{I}}\Sigma^+$ states are different. The former peaks at a lower J (\sim 26) and has a long tail extending all the way to J = 0, while the latter peaks around J = 30 and is much narrower.

There are two observable consequences of these predicted J distributions. First, the high rotational angular momentum implies that the orientation of the long-lived OD_{11}^+ fragment will not be correlated with the direction of emission of the first D_{1}^+ fragment. This is in agreement with the nearly uniform $\theta_{\mathrm{OD}_{11},\mathrm{D}_{1}}$ angular distribution seen in the experiment displayed in Fig. 2. Second, the high rotational angular momentum of the OD_{11}^+ fragment results in a barrier with respect to the dissociation limit (i.e., centrifugal

barrier) indicated in Fig. 3c, d. The internal energy of the OD_{II}^+ fragment is reflected in the distribution of $KER_{OD_{II}}$ to which all angular momenta contribute. The threshold behavior in Fig. 6b in which the KER distribution vanishes as $KER_{OD_{II}}$ goes to zero has its origin in the fact that only a small fraction of the OD_{II}^+ ions is produced with zero rotational angular momentum, and only this contribution can yield zero KER. This threshold behavior of the $KER_{OD_{II}}$ distribution predicted by the trajectory calculations is seen to be in close agreement with the experimental data.

Discussion

We studied the sequential fragmentation of water following double ionization by a single photon in unprecedented detail. The events associated with this process were separated experimentally from other fragmentation processes leading to the same final three-body channel, namely $D^+ + D^+ + O(^3P)$, using the native frames method and taking advantage of the rotation of the metastable OD_{II}^+ intermediate in the fragmentation plane. We identified two sequential-fragmentation pathways involving different electronic states and followed them step by step. Specifically, the routes are:

$$D_{2}O^{2+}(2^{1}A_{1}) \to D_{l}^{+} + OD_{ll}^{+}(b^{1}\Sigma^{+})$$
 followed by $OD_{ll}^{+}(b^{1}\Sigma^{+}) \to D_{ll}^{+} + O(^{3}P)$, (3)

and

$$\begin{split} &D_2 O^{2^+}(1^{\,1}B_1) \to D_l^+ + OD_{ll}^+(a^{\,1}\Delta) \\ &\text{followed by } OD_{ll}^+(a^{\,1}\Delta) \to D_{ll}^+ + O(^3P). \end{split} \tag{4}$$

In both pathways, the second fragmentation step involves predissociation of the OD_{ll}^+ due to spin-orbit coupling of the populated $b\,^1\!\Sigma^+$ and a $^1\!\Delta$ states with the A $^3\Pi$ state.

The results of our classical trajectory propagation on the D_2O^{2+} potential surfaces are overall in excellent agreement with the experimental data associated with both sequential fragmentation paths and the steps each one undergoes, which are detailed in Eqs. (3) and (4). We draw particular attention to our ability to calculate the internal energy of the intermediate OD_{ll}^+ molecule and probe it experimentally above the $D_{ll}^+ + O(^3P)$ dissociation limit. Likewise, the angular momentum distribution of the intermediate OD_{ll}^+ molecule has been computed and the predicted impact on the low KER distribution has been measured.

Though our methodology has been demonstrated for sequential fragmentation of water following double ionization by a single photon, it is not limited to this specific case, neither is it the only available methodology as covariance imaging analysis may also provide accurate results²⁹. In our methodology, the combination of kinematically complete momentum imaging measurements, classical trajectory simulations on the relevant PES, and the native frames method should be applicable to a wide range of polyatomic molecules as long as the energy deposited in the system is known and there is a clear signature enabling identification of sequential fragmentation from other processes, like the rotation of the intermediate molecular fragment in this case. This methodology enhances our capabilities for exploring molecular reaction dynamics on the PES around asymmetric stretch that is commonly the path for forming an intermediate molecular fragment en route to sequential fragmentation. The observation of sequential steps in a molecular dissociation reaction via their unambiguous signature in the momenta of the fragments has added the dimension of time evolution to an essentially time-independent measurement.

Methods

The methodology that enables us to compare theory and experiment step by step and state selectively is based on three main components, described briefly below. Further details are provided in the references.

Theory

The PESs of the water dication are computed using the MOLPRO^{30,31} quantum chemistry suite in internally contracted multireference configuration interaction (icMRCI) methods at the configuration interaction singles and doubles level relative to the reference space including Davidson correction to the energy, by Gervais et al.²⁶ and Streeter et al.²³. The full dimensional surfaces are then fitted using a linear least squares fit to a functional form developed by Gervais et al.²⁶. Those studies established the branching ratios between two-body (D⁺ + OD⁺) and three-body (D⁺ + D⁺ + O) breakup on each potential surface of the nine states of the water dication that can be accessed at the photon energy used in our experiment.

Three states of D_2O^{2+} , the 1^1A_1 , 2^1A_1 , and 1^1B_1 states, shown in Fig. 1a, produce the $b^1\Sigma^+$ state (which correlates with the 2^1A_1 state) and the two components of the degenerate $a^1\Delta$ state of $OD_{ll}^{+25,26}$, both shown in Fig. 1b. However, only two of those, the 2^1A_1 and 1^1B_1 states, produce the diatomic ion with enough internal energy to dissociate appreciably by this mechanism and be seen in one-photon double photoionization, as is suggested by Fig. 5 of ref. 26.

We model the reaction dynamics by propagating ensembles of classical trajectories on the relevant potential surface for a few picoseconds and then evaluate the OD_{II}^+ population. The computational approach used here is the same as that of our previous studies^{23,24}. The Wigner phase space density for the initial vibrational state is propagated on the dication PESs using classical trajectories, and the final momenta and internal energy distributions are evaluated classically from this ensemble of trajectories. This approach has been benchmarked for three-body breakup in this system by excellent agreement of the final momentum distribution with momentum imaging experiments^{23,24}. For the internal energy distributions of the OH fragment in the two-body channels, the accuracy of the classical Wigner method was confirmed by Gervais et al.²⁶ as well as by the agreement with the experiment displayed in Fig. 6. Such an ensemble of trajectories is the basis of the well-studied Wigner semiclassical method³²⁻³⁴ for predicting final quantum state distributions. For the dissociative dynamics in this case, however, quantum effects are unimportant and a purely classical analysis suffices.

The molecule is initially in its ground vibrational state and undergoes a Franck–Condon transition to the doubly ionized excited state. The initial conditions for the 1,000,000 computed classical trajectories, for each D_2O^{2+} state we consider, are sampled from the corresponding Wigner distribution, assuming that the ground vibrational state can be represented by a direct product wave function of the normal modes. At the end of the propagation the internal energy, and the rotational angular momentum, J, of the OD_{II}^+ fragment, are computed from the Cartesian momenta and coordinates of the atoms together with the value of the potential energy. The OD_{II}^+ is considered to be bound if the total energy of an $O-D_{II}^+$ pair is less than the J-dependent barrier to dissociation associated with the relevant final states of OD_{II}^+ , specifically the $D_{II}^+ + O(^ID)$ limit shown in Fig. 1b.

As stated above, the second fragmentation step involves predissociation of the b $^1\Sigma^+$ and a $^1\Delta$ states of the intermediate OD_{II}^+ ion due to spin-orbit coupling with its A $^3\Pi$ state. The central dynamical assumption of our treatment takes advantage of the relatively short lifetimes for this predissociation via a nonadiabatic transition to the A $^3\Pi$ state compared to the fragments' flight time in the experimental setup. We therefore assume in our classical trajectory calculations that all OD_{II}^+ ions, with internal energy above the $D_{II}^+ + O(^3P)$ dissociation limit, predissociate within a few picoseconds 25,26 . For example, all trajectories in the b $^1\Sigma^+$ state having zero rotational angular momentum and with vibrational energies between the two horizontal dashed lines in Fig. 1b, labeled appearance window, are assumed to lead to $D_{II}^+ + O$ fragments. Such an appearance window was recently found to play an important role in another polyatomic molecule, i.e., in the valence

photo-double ionization of ammonia³⁵. Nonzero rotational angular momentum adds a centrifugal barrier to this picture for all three states of OD_{II}^+ in Fig. 1b, modifying the assumption about the dissociating rovibrational states to those with energy above the barrier leading to the $D_{II}^+ + O(^3P)$ dissociation limit, and therefore the appearance window shifts. For simplicity, tunneling through the centrifugal barrier for $J \neq 0$ is neglected in our treatment.

Experimental method

To identify, separate, and follow all electronic states involved in the dissociation sequence, a kinematically complete experiment is required, and that entails the determination of the final momenta of all fragments from each molecule. In the present case, we measure two electrons and two deuterons in coincidence and determine their final momenta by solving their classical equations of motion in the COLTRIMS setup⁵⁻⁷. Then, we employ momentum conservation to evaluate the final momentum of the neutral oxygen. To avoid artifacts caused by the identical D⁺ fragments, we follow the common practice and randomize their time order, i.e., flip the order of the 1st and 2nd D⁺ hits randomly for half of the events. It is worth noting that the few picoseconds lifetime of the OD⁺ intermediate molecule is long enough to completely deplete the populated OD⁺ states above the D⁺ + O(³P) dissociation limit, and short enough (sub nanosecond) to avoid distortion of the measured momentum images.

It is also essential to know how much energy is deposited in each water molecule. To accomplish that we doubly ionize the water molecule by single-photon absorption, using a 61 eV narrow bandwidth (50 meV) synchrotron light pulse provided by the Advanced Light Source (ALS), thereby producing water dications 24.1 eV above the $D^+ + D^+ + O(^3P)$ dissociation limit. Using this photon energy together with the measured kinetic energy of both electrons and all the other fragments allows the selection of only events ending on a specific dissociation limit^{23,24}. Using 61 eV photons, which are below the triple ionization potential of water, also eliminates the need to filter out $D^+ + D^+ + O^+$ events.

The expected total energy release, $E_{\rm release}$, is computed by subtracting the complete dissociation energy of the heavy water dication into D⁺ + D⁺ + O(³P) from the measured photon energy used in our experiment. The accumulated error in the measured $E_{\rm release}$ and photon energy, as well as uncertainties in the complete dissociation energy of water recommended by NIST, add up to an estimated uncertainty of the order of the energy shift needed to match the measured spectrum shown in Fig. 4 (see Supplementary Note 2 for further details).

Heavy water, D_2O , is chosen over H_2O in order to circumvent contributions from double ionization of H_2O and H_2 molecules, both common residual gases in ultra-high vacuum systems, also producing $H^+ + H^+ + 2e^-$. These residual gases are much warmer than the COLTRIMS jet and are present throughout the light-beam propagation direction, therefore contaminating the momentum imaging, especially when one cannot use momentum conservation to eliminate them, as is the case for the breakup channel of interest. The D_2O target choice should not affect the fragmentation pathways since each water isotopologue is expected to undergo similar dynamics.

Native frames analysis

In the native frames method 21,22 , which we employ to analyze the three-body breakup, the key ingredient is the use of the conjugate momenta of the Jacobi coordinates, where these coordinates describe the relative positions of the three fragments. In the case of D_2O , shown schematically in Fig. 2b, the conjugate momentum corresponding to the first fragmentation step is given by

$$\mathbf{p}_{\text{OD}_{1},\text{D}_{1}} = \frac{m_{\text{OD}}}{M} \mathbf{P}_{\text{D}_{1}} - \frac{m_{\text{D}}}{M} \left[\mathbf{P}_{\text{D}_{1}} + \mathbf{P}_{\text{O}} \right], \tag{5}$$

where \mathbf{P}_{D} and \mathbf{P}_{O} are the measured momenta of the D⁺ and O fragments, respectively, m_{D} is the mass of D⁺, m_{OD} is the mass of OD_{II}, and M is the mass of the D₂O²⁺.

Similarly, the conjugate momentum associated with the second step is

$$\mathbf{p}_{\mathrm{OD}_{11}} = \mu_{\mathrm{OD}} \left[\frac{\mathbf{P}_{\mathrm{D}_{11}}}{m_{\mathrm{D}}} - \frac{\mathbf{P}_{\mathrm{O}}}{m_{\mathrm{O}}} \right], \tag{6}$$

where $\mu_{\rm OD}$ is the reduced mass of ${\rm OD_{II}}$. Finally, the angle between the two conjugate momenta, $\theta_{{\rm OD_{II}},{\rm D_I}}$, is computed from the dot product of these vectors. Equations (5) and (6) are the conjugate momenta of the Jacobi coordinates for the ${\rm D_I}+{\rm OD_{II}}$ arrangement, and they can be used to compute the KER in each fragmentation step. For example, the KER in the second step (used in Fig. 2) is given by ${\rm KER_{OD_{II}}}=p_{\rm OD_{II}}^2/2\,\mu_{\rm OD}$.

The second ingredient needed to separate sequential fragmentation from other competing processes is a clear signature distinguishing it from the others. As mentioned above, rotation of the intermediate OD_{II} in the fragmentation plane, persisting long enough to wipe out any initial angular preference, leads to a distinct nearly uniform $N(\theta_{\mathrm{OD_{11},D_1}})$ angular distribution. The KER in the second fragmentation step, KER_{OD_n} , combined with the molecular structure of this intermediate molecule, provides an additional constraint for identifying sequential breakup. Therefore, to identify and separate the sequential fragmentation via an OD_{II}^+ intermediate, we plot in Fig. 2a all the measured D⁺ + D⁺ + O events as a function of KER_{OD_n} and θ _{OD_n,D_t}, where we arbitrarily designate one of the two D⁺ fragments (denoted D_i+)-ejected first-a correct coin-flip assignment for half of the sequential events. Then, we identify the (properly assigned) sequential breakup as the uniform angular stripe marked by the dashed-magenta rectangular boundary in the figure. Note that the KER distribution of this stripe matches the predicted 0-2.25 eV range^{25,26}, indicated by the appearance window in Fig. 1b.

Then, we use the identified sequential events within the dashed-magenta boundary in Fig. 2a to create equivalent events by randomly rotating them to smaller angles until the whole range has a uniform yield within the uncertainty of the data. It is important to note that any other information from each event, like $KER_{OD_{II}}$, is preserved by this reconstruction algorithm²². The resulting complete reconstructed angular distribution of the $D_2O^{2+} \rightarrow D_I^+ + OD_{II}^+$ followed by $OD_{II}^+ \rightarrow D_{II}^+ + O$ sequential fragmentation is shown in Fig. 2c.

Finally, in Fig. 2d we present the $N(KER_{OD_1}, \theta_{OD_1,D_1})$ distribution—a similar distribution to that shown in panel (c) but with the D+ fragmentats associated incorrectly with their breakup-step order. Specifically, we are plotting sequential breakup occurring via the OD, intermediate in the frame assuming an OD_i intermediate. To generate such a distribution with certainty, we use the events identified as sequential fragmentation via $D_I^+ + OD_{II}^+$ and shown in Fig. 2c, but analyze them as if the D_{II} was ejected first, i.e., using the reference frames that are not associated with the relevant center-of-mass of each breakup step. In other words, their momenta are calculated in the other Jacobi coordinate arrangement, namely $\boldsymbol{p}_{OD_1,D_{11}}$ and $\boldsymbol{p}_{OD_1}.$ One can clearly see that the two distributions, shown separately in panels (c) and (d) are significantly different from each other, and both are also visible in the all-events data shown in panel (a). Hence, one can associate each detected D+ with the relevant fragmentation step.

Data availability

The data that support the findings of this study are available in this article and its Supplementary Information. The raw data are available from the corresponding authors upon request. Source data are provided with this paper.

References

- Marangos, J. P. The measurement of ultrafast electronic and structural dynamics with X-rays. *Phil. Trans. R. Soc. A: Math., Phys. Eng. Sci.* 377, 20170481 (2019).
- Geneaux, R., Marroux, H. J. B., Guggenmos, A., Neumark, D. M. & Leone, S. R. Transient absorption spectroscopy using high harmonic generation: A review of ultrafast X-ray dynamics in molecules and solids. *Phil. Trans. R. Soc. A: Math., Phys. Eng. Sci.* 377, 20170463 (2019).
- 3. Ware, M. R., Glownia, J. M., Natan, A., Cryan, J. P. & Bucksbaum, P. H. On the limits of observing motion in time-resolved X-ray scattering. *Phil. Trans. R. Soc. A: Math., Phys. Eng. Sci.* **377**, 20170477 (2019).
- 4. Jahnke, T. et al. Inner-shell-ionization-induced femtosecond structural dynamics of water molecules imaged at an X-ray free-electron laser. *Phys. Rev. X* 11, O41044 (2021).
- Ullrich, J. et al. Recoil-ion momentum spectroscopy. J. Phys. B 30, 2917 (1997).
- Dörner, R. et al. Cold target recoil ion momentum spectroscopy: A 'momentum microscope' to view atomic collision dynamics. *Phys. Rep.* 330, 95 (2000).
- Ullrich, J. et al. Recoil-ion and electron momentum spectroscopy: Reaction-microscopes. Rep. Prog. Phys. 66, 1463 (2003).
- Allum, F. et al. Coulomb explosion imaging of CH₃I and CH₂CII photodissociation dynamics. J. Chem. Phys. 149, 204313 (2018).
- Corrales, M. E., González-Vázquez, J., de Nalda, R. & Bañares, L. Coulomb explosion imaging for the visualization of a conical intersection. J. Phys. Chem. Lett. 10, 138 (2019).
- Crane, S. W. et al. Nonadiabatic coupling effects in the 800 nm strong-field ionization-induced Coulomb explosion of methyl iodide revealed by multimass velocity map imaging and ab initio simulation studies. J. Phys. Chem. A 125, 9594 (2021).
- 11. Endo, T. et al. Capturing roaming molecular fragments in real time. Science **370**, 1072 (2020).
- Liu, Y. et al. Spectroscopic and structural probing of excited-state molecular dynamics with time-resolved photoelectron spectroscopy and ultrafast electron diffraction. *Phys. Rev. X* 10, 021016 (2020).
- 13. Hishikawa, A., Hasegawa, H. & Yamanouchi, K. Sequential three-body Coulomb explosion of CS_2 in intense laser fields appearing in momentum correlation map. *Chem. Phys. Lett.* **361**, 245 (2002).
- Savee, J. D., Mozhayskiy, V. A., Mann, J. E., Krylov, A. I. & Continetti, R. E. The role of excited-state topology in three-body dissociation of sym-triazine. *Science* 321, 826 (2008).
- 15. Neumann, N. et al. Fragmentation dynamics of $CO_2^{3^+}$ investigated by multiple electron capture in collisions with slow highly charged ions. *Phys. Rev. Lett.* **104**, 103201 (2010).
- Wu, C. et al. Nonsequential and sequential fragmentation of CO₂³⁺ in intense laser fields. *Phys. Rev. Lett.* 110, 103601 (2013).
- Wales, B. et al. Coulomb imaging of the concerted and stepwise break up processes of OCS ions in intense femtosecond laser radiation. J. Elect. Spectr. Rel. Phenom. 195, 332 (2014).
- 18. Guillemin, R. et al. Selecting core-hole localization or delocalization in CS_2 by photofragmentation dynamics. *Nat. Commun.* **6**, 6166 (2015).
- Ablikim, U. et al. Isomer-dependent fragmentation dynamics of inner-shell photoionized difluoroiodobenzene. *Phys. Chem. Chem. Phys.* 19, 13419 (2017).
- Ding, X. et al. Ultrafast dissociation of metastable CO²⁺ in a dimer. Phys. Rev. Lett. 118, 153001 (2017).
- Rajput, J. et al. Native frames: Disentangling sequential from concerted three-body fragmentation. *Phys. Rev. Lett.* 120, 103001 (2018).
- T., Severt, Imaging Light-Induced Molecular Fragmentation Dynamics. Ph.D. thesis, Kansas State University (2021).

- Streeter, Z. L. et al. Dissociation dynamics of the water dication following one-photon double ionization. I. Theory. *Phys. Rev. A* 98, 053429 (2018).
- Reedy, D. et al. Dissociation dynamics of the water dication following one-photon double ionization. II. Experiment. *Phys. Rev. A* 98, 053430 (2018).
- de Vivie, R., Marian, C. M. & Peyerimhoff, S. D. Spin-forbidden transitions in the presence of an intersystem crossing: Application to the b ¹Σ* state in OH*. Chem. Phys. 112, 349 (1987).
- Gervais, B. et al. The H₂O²⁺ potential energy surfaces dissociating into H⁺/OH⁺: Theoretical analysis of the isotopic effect. *J. Chem. Phys.* 131, 024302 (2009).
- Shen, Z., Wang, E., Gong, M., Shan, X. & Chen, X. Fragmentation dynamics of carbonyl sulfide in collision with 500 eV electron. J. Chem. Phys. 145, 234303 (2016).
- Weber, T. et al. Complete photo-fragmentation of the deuterium molecule. Nature 431, 437 (2004).
- Cooper, G. A., Alavi, S. T., Li, W., Lee, S. K. & Suits, A. G. Coulomb explosion dynamics of chlorocarbonylsulfenyl chloride. *J. Phys. Chem. A* 125, 5481 (2021).
- Werner, H.-J., Knowles, P. J., Knizia, G., Manby, F. R. & Schütz, M. Molpro: A general-purpose quantum chemistry program package. WIREs Comput. Mol. Sci. 2, 242 (2012).
- 31. Werner, H.-J. et al. Molpro, version 2015.1, a package of ab-initio programs, 2015, see http://www.molpro.net (2012).
- Brown, R. C. & Heller, E. J. Classical trajectory approach to photodissociation: The Wigner method. J. Chem. Phys. 75, 186 (1981).
- 33. Henriksen, N. E., Engel, V. & Schinke, R. Test of the Wigner method for the photodissociation of symmetric triatomic molecules. *J. Chem. Phys.* **86**, 6862 (1987).
- Arbelo-González, W., Bonnet, L. & García-Vela, A. Semiclassical Wigner theory of photodissociation in three dimensions: Shedding light on its basis. J. Chem. Phys. 142, 134111 (2015).
- Larsen, K. A. et al. Photoelectron and fragmentation dynamics of the H*+H* dissociative channel in NH₃ following direct single-photon double ionization. *Phys. Rev. Res.* 2, 043056 (2020).

Acknowledgements

We thank the staff at the Advanced Light Source for operating the beamline and providing the photon beam. Work at LBNL was performed under the auspices of the U.S. Department of Energy (DOE), Office of Science, Office of Basic Energy Sciences, Chemical Sciences, Geosciences, and Biosciences Division under Contract No. DEACO2-05CH11231 (a grant that also supported Z.L.S., W.I., K.A.L., E.G.C., M.M.B., D.S.S., R.R.L., T.W., and C.W.McC.), using the Advanced Light Source (ALS), the National Energy Research Computing Center (NERSC), a DOE Office of Science User Facility, and the Lawrencium computational cluster resource provided by the IT Division at the LBNL. JRML personnel (namely, T.S., B.J., and I.B.-I.) were supported by Grant No. DE-FGO2-86ER13491 from the same funding agency. UNR personnel (specifically, B.G. D.R., D.C., and J.B.W.) were supported by National Science Foundation (NSF) grant No. 1807017. B.G. was also supported by the DOE Office of Science, Office of Workforce Development for Teachers

and Scientists, Office of Science Graduate Student Research (SCGSR) program, which is administered by the Oak Ridge Institute for Science and Education for the DOE under Contract No. DE-SCOO14664. R.D. and D.T. acknowledge support from Deutsche Forschungsgemeinschaft via Sonderforschungsbereich 1319 (ELCH). A.G. was supported by the ALS through a Doctoral Fellowship in Residence.

Author contributions

W.I., T.S., K.A.L., D.C., A.G., D.T., B.G., D.R., R.S., E.G.C., B.J., M.M.B., I.B.-I., D.S.S., and T.W. Planned, set up, and performed the experiment; T.S. and W.I. conducted the native frames and COLTRIMS data analysis, respectively; Z.L.S. and R.R.L. performed calculations; J.B.W., A.L., D.S.S., T.W., C.W.McC., and I.B.-I. mentored students and post-docs; T.S., Z.L.S., T.W., R.R.L., C.W.McC., and I.B.-I. prepared the manuscript, which all co-authors approved.

Competing interests

The authors declare no competing interests.

Additional information

Supplementary information The online version contains supplementary material available at https://doi.org/10.1038/s41467-022-32836-6.

Correspondence and requests for materials should be addressed to Thorsten Weber, C. William McCurdy or Itzik Ben-Itzhak.

Peer review information Nature Communications thanks Sylvain Maclot, and the other, anonymous, reviewer(s) for their contribution to the peer review of this work.

Reprints and permission information is available at http://www.nature.com/reprints

Publisher's note Springer Nature remains neutral with regard to jurisdictional claims in published maps and institutional affiliations.

Open Access This article is licensed under a Creative Commons Attribution 4.0 International License, which permits use, sharing, adaptation, distribution and reproduction in any medium or format, as long as you give appropriate credit to the original author(s) and the source, provide a link to the Creative Commons license, and indicate if changes were made. The images or other third party material in this article are included in the article's Creative Commons license, unless indicated otherwise in a credit line to the material. If material is not included in the article's Creative Commons license and your intended use is not permitted by statutory regulation or exceeds the permitted use, you will need to obtain permission directly from the copyright holder. To view a copy of this license, visit http://creativecommons.org/licenses/by/4.0/.

© The Author(s) 2022